ADVANCED SUSTAINABLE SYSTEMS
www.advsustainsys.com

Can Aluminum Impurity from Current Collectors Upgrade Spent $Li_{1-x}CoO_2$ into a High-Performing Cathode for Lithium-Ion Batteries?

Lingyu Kong, Duo Wang, Fang Zhang, Xianwei Hu, Aimin Liu, Yulong Cao, Zhongning Shi, Amr. M. Abdelkader, and Ali Reza Kamali**

The recycling of spent lithium-ion batteries (LIBs) is gaining considerable attention for its potential to address resource scarcity and mitigating environmental pollution. Therefore, the recycling process of spent LIBs should be simple and efficient and minimize the input of raw materials. This work uses residual Al impurities from current collectors combined with high-temperature Li supplementation to directly repair spent $Li_{1-x}CoO_2$ cathode into regenerated materials enhanced with Al doping and LiF coating without additional synthesis steps or cost. The regenerated materials demonstrate an enhanced electrochemical performance compared to commercial cathode material. The modified materials exhibit a notable initial discharge capacity of 181 mA h g^{-1}, with a commendable capacity retention of 80.4% after 400 cycles at a 4.5 V cut-off voltage. The improved electrochemical performance is attributed to the enhanced crystalline and structural stability of the regenerated materials. Furthermore, the superiority of spent materials over commercial materials modification is clarified for the first time through characterizations and theoretical calculations due to their degraded crystalline structure and abundant Li vacancies. This up-cycling strategy not only contributes to sustainable waste management of spent LIBs but also provides a potential "shortcut" for advancing next-generation high-performance batteries.

1. Introduction

Lithium-ion battery (LIB) technology is the most representative energy storage approach, broadly applied in electric vehicles and stationary storage applications due to its outstanding electrochemical characteristics.[1,2] The widespread adoption of LIBs, while providing notable benefits, will inevitably pose urgent and significant challenges to society upon reaching the end of their lifespan.[3,4] On one hand, the improper disposal of spent LIBs would cause serious environmental issues, due to the presence of potentially toxic substances.[5,6] On the other hand, spent LIBs contain various valuable metals including Li, Co, Ni, and Mn, which are worth recycling to solve the dilemma of the uneven availability and limited resources of such critical elements on the Earth.[7,8] Therefore, it is crucial to develop advanced recycling methods for spent batteries to realize the sustainable development of LIBs.

Pyrometallurgy and hydrometallurgy or their combination are conventional methods for recovering valuable metals from spent LIBs.[9–11] But they still inevitably face the challenges of high energy consumption, harmful gas emissions, complicated procedures, high chemical reagent consumption, and secondary pollution.[12–14] In addition, both pyrometallurgical and hydrometallurgical methods break down the structure of

L. Kong, D. Wang, F. Zhang, X. Hu, A. Liu, Z. Shi, A. R. Kamali
Key Laboratory for Ecological Metallurgy of Multimetallic Mineral (Ministry of Education)
Northeastern University
Shenyang 110819, P. R. China
E-mail: ali@mail.neu.edu.cn

L. Kong, A. M. Abdelkader
Department of Design and Engineering
Bournemouth University
Talbot Campus
Poole BH12 5BB, UK
E-mail: aabdelkader@bournemouth.ac.uk

Y. Cao
The State Key Laboratory of Refractories and Metallurgy
Wuhan University of Science and Technology
Wuhan 430081, P. R. China

A. R. Kamali
Energy and Environmental Materials Research Centre (E^2MC)
School of Metallurgy
Northeastern University
Shenyang 110819, P. R. China

The ORCID identification number(s) for the author(s) of this article can be found under https://doi.org/10.1002/adsu.202400198

DOI: 10.1002/adsu.202400198

the cathode materials into lower-value constituents, considering that the composition and structure of cathode materials have considerable value embedded in manufactured LIBs, and such methods inevitably result in the loss of these embedded values.[15–17]

To overcome the above-mentioned disadvantages, some direct recycling strategies with minimal energy and environmental impact have been proposed in recent years, such as solid-state synthesis, hydrothermal treatment, molten salt, and electrochemical methods.[18] Among them, solid-phase synthesis has shown great potential due to its excellent economic and environmental advantages.[19] The lithium salts are used to supplement the components of the degraded cathode materials and repair virgin structure and morphology directly without chemical decomposition. Gao et al.[20] used the solid-state synthesis method to directly regenerate the structure of spent $LiCoO_2$ (LCO) materials and compared the effects of different lithium salts, mole ratio of Li to Co, and calcination temperatures on the structure of regenerated compounds. Consequently, a perfect layered LCO structure could be regenerated using Li_2CO_3 as the Li source at a mole ratio of 1 at the calcination temperature of 800 °C. Chi et al.[21] fully reutilized surface lithium compound residues as a lithium supplement to reconstruct the crystal structure of NCM combined with an over-discharging pre-treatment. No additional compounds were induced during the direct calcination process, and the lithium content could be efficiently reused, alleviating the problem of resource shortage. In addition, Ji et al.[22] used 3,4-dihydroxybenzonitrile dilithium as a lithium source to restore spent $LiFePO_4$ cathode by solid-state synthesis. The degraded particles are well coupled with the functional groups of organic lithium salts, with cyano groups forming a reducing atmosphere to inhibit the Fe (III) phase. At the same time, the pyrolysis of salt produces an amorphous conductive carbon layer that covers the $LiFePO_4$ particles, improving the transfer kinetics of Li^+ and electrons.

The pursuit of high-voltage cathode materials is a crucial task in developing next-generation high-energy LIBs.[23] In this regard, the preparation of high-voltage electrodes using spent electrode materials is a viable approach, involving the direct repair of spent materials combined with doping or coating of regenerated materials. He et al.[24] used Mn^{2+}, Co^{2+}, Ni^{2+}, and Li^+ acetates to regenerate and modify spent LCO materials by coating layered lithium-rich manganese-based materials using a sol-gel method. The regenerated composites showed an initial capacity of 197.1 mA h g^{-1} at 0.1 C, and ≈95.8% retention (1 C) after 100 cycles under 3.0–4.5 V due to the high-voltage stability and high energy density of the layered lithium-rich manganese-based materials. Fan et al.[25] employed solid-state synthesis and Mg doping to reconstruct a high-voltage cathode from spent materials. The recovered material containing 5% Mg showed a high discharge capacity of 202.9 mA h g^{-1} (0.2 C) within the voltage window 3.0–4.6 V. Wu et al.[26] regenerated a high-performance Na-doped LCO using spent LIBs through re-lithiation and structural modification. The prepared $Li_{0.99}Na_{0.01}CoO_2$ cathode displayed an excellent discharge capacity of 180 mA h g^{-1} (1 C) at the voltage range of 3–4.5 V. However, the high-temperature doping and coating inevitably increase the energy consumption and raw material input and complicate the recycling process, which contradicts the advantages of direct repair methods.

Therefore, direct in situ regeneration of high-voltage cathode materials from spent LIBs can provide significant advantages in the realm of next-generation high-energy-density LIBs in terms of both economic efficiency and environmental sustainability. In this work, high-voltage cathode materials are prepared by the direct repair of spent LCO materials through a simple and efficient solid-state synthesis. By examining the phase, morphology, crystal structure, and surface chemical state of the regenerated materials, in situ modification can be realized through Al doping and LiF coating while the defective crystalline structure of the spent LCO materials is repaired. Based on these observations combined with theoretical calculations, it is proved that spent LCO materials have a greater potential to be used in such an efficient preparation process of these high voltage cathode materials in comparison with commercial virgin electrode materials due to their structural characteristics of easy modification.

2. Results and Discussion

2.1. Solid-Phase Synthesis Process of Spent Materials and Characterization

The solid-state synthesis regeneration process was characterized in detail to fully understand the repair and regeneration process of SLCO materials, as shown in **Figure 1**. The TG curve of the SLCO-Li_2CO_3 mixture (Figure 1a) shows three obvious weight loss stages: The first weight loss region, 30–500 °C, is ascribed to the oxidization of the acetylene black, which accounts for 0.4 wt%. A significant endothermic peak is observed at 701 °C in the DSC curve of Figure 1a, accompanied by a 7.3% weight loss in the temperature range of 500–712 °C, indicating the decomposition of Li_2CO_3. As noticeable, when mixed with SLCO material, Li_2CO_3 begins to decompose at 500 °C, indicating that the repair process of SLCO material mainly occurs at this stage. However, according to the Li_2CO_3-Li_2O phase diagram and Gibbs free energy calculations (Figure 1b,c), Li_2CO_3 can only decompose when heated to ≈720 °C. This is because SLCO material has a "catalytic effect" on the decomposition of Li_2CO_3, which is caused by its edge defects.[27] No obvious endothermic and exothermic peaks are observed in the third region, and the mass decreases with the increase in temperature, which may be related to the volatilization of the generated Li_2O.

Ex situ XRD was used to investigate the phase and crystal structure changes of SLCO material during the solid-state synthesis process, as shown in Figure 1d. The Co_3O_4 impurity peak in SLCO material indicates that the repeated (de)intercalation process leads to the loss of Li, resulting in irreversible conversion reactions. The ICP results confirmed the loss of Li in the SLCO material and the trace Al residue (0.17 wt%) after the pretreatment process, as shown in Table S1 (Supporting Information). When SLCO was calcined at 850 °C for 3 h, the impurity phase of Co_3O_4 completely disappeared, indicating the effectiveness of the regeneration process. Furthermore, the shift of the (003) peak represents the change in the SLCO crystal structure (Figure 1e). As the regeneration time increases, the (003) peak first shifts to lower angles, corresponding to an increase in the lattice spacing between CoO_6 (c-distance) caused by the Li intercalation. It is worth noting that the possible Al doping in the SLCO crystal structure also has a slight effect on the interplanar spacing.

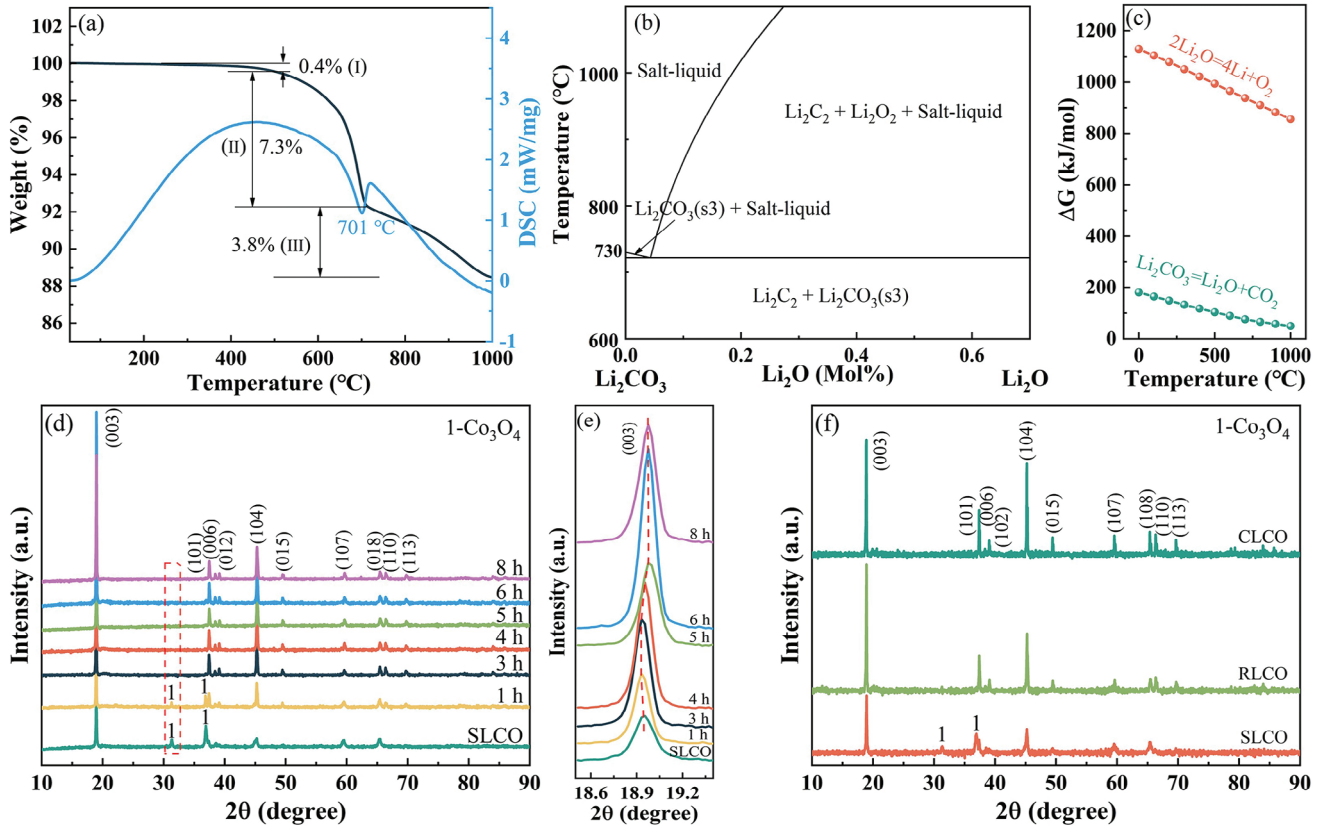

Figure 1. Regeneration of SLCO to RLCO. a) TG-DSC curves of the mixture of SLCO and Li_2CO_3. b) Li_2CO_3–Li_2O phase diagram (calculated by FactSage software). c) Gibbs free energies of possible reactions occurring during the regeneration process. d) and e) Ex situ XRD patterns of regeneration process. f) XRD pattern of SLCO, RLCO, and CLCO.

The (003) peak shifts back to higher angles subsequently, indicating the end of the regeneration reaction. The crystal structure of RLCO material keeps a well-defined hexagonal α-$NaFeO_2$ layered structure with an $R\bar{3}m$ space group, consistent with CLCO (Figure 1f). In addition, Rietveld refinement was performed to further analyze XRD patterns, as shown in Figures S1 and S2 and Table S2 (Supporting Information). The calculated c value increases first and then decreases with the extension of regeneration time, and the impurity content of Co_3O_4 decreases from 17.57% in SLCO to 1.27% (1 h) and 0 (3 h), which is consistent with the results of ex situ XRD analysis. Moreover, the c/a value of RLCO is over 4.99 (consistent with CLCO), indicating the formation of a well-layered structure after regeneration.

The morphology and structure changes of SLCO cathode material were investigated by SEM and TEM, as shown in **Figure 2**. The particle surface of SLCO is rough and shows a large number of microcracks due to the loss of Li and inhomogeneous volume changes and internal mechanical stresses caused by the continuous intercalation/de-intercalation of Li, as shown in Figure 2a. In addition, the TEM results further indicate that its crystal structure is severely degraded, and clear crystal regions cannot be observed (Figure 2d). The loss of Li leads to local phase transitions near the surface from ordered layered structure to disordered spinel structure (Co_3O_4), which is consistent with the XRD analysis results. However, the RLCO particles show a smooth surface, uniform distribution of elements, complete layered structure, and clear crystalline domains, consistent with CLCO, which means that the crystal structure of SLCO material is restored to the level of commercial materials (Figure 2b,c,e,f). Based on the above analysis, during the solid-state regeneration process, Li_2CO_3 is first attached to the microcrack and then is thermally decomposed into Li_2O under the catalysis effect of spent materials. Subsequently, while Li_2O reacts with the Co_3O_4 impurity phase present in spent materials, Li^+ diffuses inside the spent material and refills Li vacancies to regenerate LCO crystals at high temperatures. The newly generated LCO particles gradually grow and cover all the microcracks during the heating process, thus regenerating structurally intact LCO particles with a smooth surface. Furthermore, RLCO material shows a larger interplanar spacing compared with CLCO, which may be related to the trace doping of Al in the layered structure.

To further verify whether Al doping occurs during the regeneration process, XPS high-resolution spectra were recorded to characterize different materials, as shown in **Figure 3**. The wide-scan XPS spectra reveal the similar elemental composition of SLCO and RLCO materials, as shown in Figure S3 (Supporting Information). As shown in the spectra of Co 2p of SLCO and RLCO (Figure 3a,d), the binding energies located at 779.48 and 794.08 eV are attributed to Co^{3+}, while the binding energies located at 781.28 and 795.58 eV correspond to Co^{2+}.[28] In addition, the O 1s XPS spectra of SLCO and RLCO can be decomposed into two peaks at 529.08 and 531.38 eV, corresponding

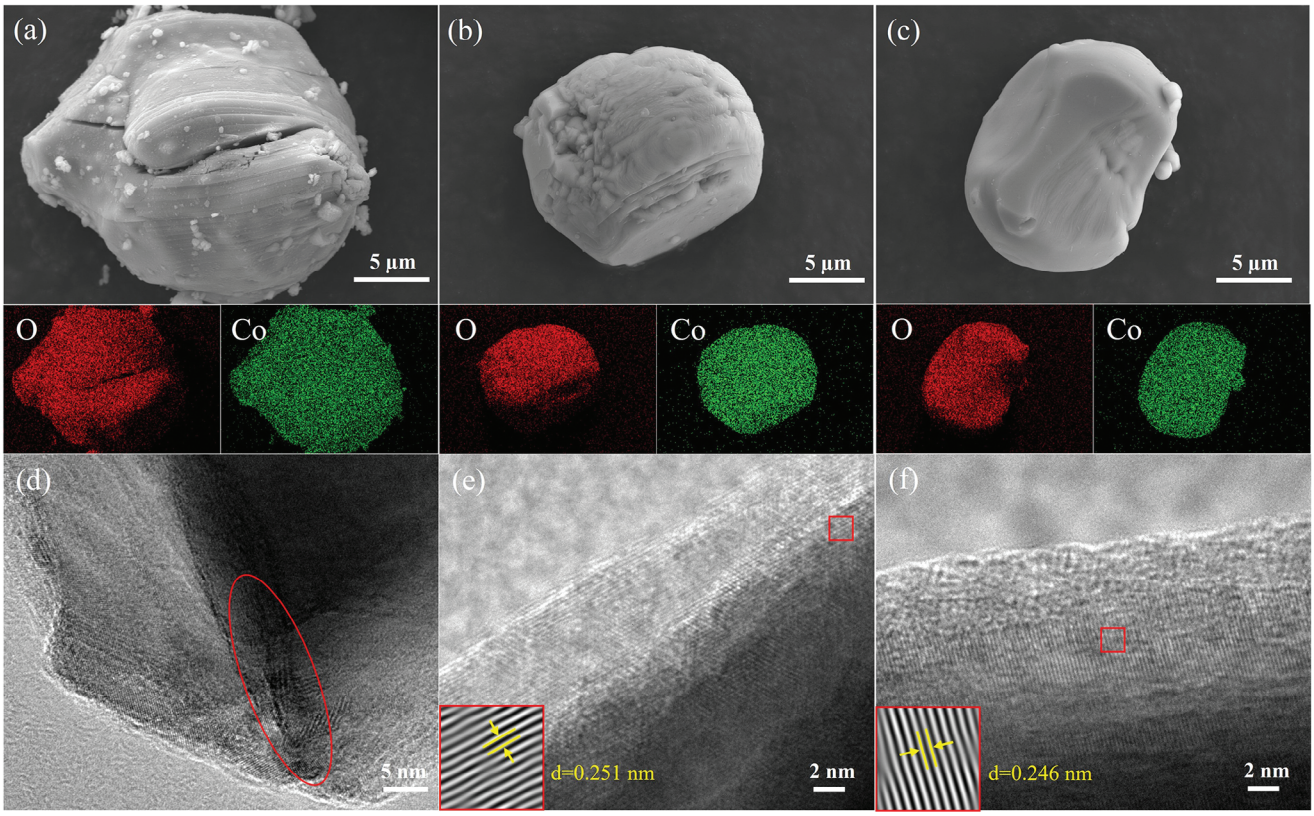

Figure 2. Microstructural characterization for the LCO materials. SEM images and corresponding element distribution of SLCO a), RLCO b), and CLCO c). TEM images of SLCO d), RLCO e), and CLCO f).

to lattice oxygen originating from the layered crystalline structure (O—TM, TM: transition metal) and O impurities (active oxygen species O^{2-}, active oxygen species O^{1-}, or/and CO_3^{2-}), respectively (Figure 3b,e).[29] Combined with the C 1s XPS spectra (Figure S4, Supporting Information), O impurities mainly include active oxygen species O^{1-} and CO_3^{2-}. Moreover, the Co^{3+} content increases from 65.26% in SLCO to 74.96% in RLCO, and the increase of O—TM proportion indicates surface reorganization and lattice oxygen restoration, reflecting the effectiveness of structure regeneration. Compared with SLCO, the Al 2p XPS spectrum of RLCO shows the Al—O peak at 71.18 eV, as shown in Figure 3c,f. In addition, EDS mapping of a random-selected RLCO particle confirms the uniform distribution of Al element (Figure S5, Supporting Information). Combined with ex situ XRD and TEM analysis, it is confirmed that the RLCO material is doped with Al during the solid-state regeneration process. In addition, compared with CLCO material (Figure 3i), the F 1s XPS spectra of SLCO and RLCO only include LiF peak at 684.98 eV,[30] which confirms the removal of binder residuals and the formation of LiF coating, as shown in Figure 3g,h. The formation of LiF coating may be due to the long cycle residue (cathode electrolyte interface layer), and decomposition of polyvinylidene difluoride (PVDF) during the pretreatment process. PVDF is already known to be a low temperature fluorinating reagent for metal oxides, and HF produced by thermal decomposition of PVDF leads to the formation of LiF on the surface of SLCO particles. A comparative experiment was conducted to verify the fluorination effect of PVDF by mixing CLCO materials and PVDF (details are provided in the Supporting Information). As shown in Figure S6 (Supporting Information), it can be confirmed that PVDF can fluorinate the surface of LCO particles to generate LiF during the pretreatment process, and the calcined product remains in the LCO phase. Moreover, the volatilization temperature of LiF is very high (1100–1200 °C), and it will stably exist on the surface of particles during the regeneration process. Therefore, the solid-state synthesis method discussed here can not only effectively repair the crystal structure of spent LCO materials, but also lead to the material's modification through Al doping and LiF coating. RLCO material has a significant potential as a high-voltage cathode, as discussed in the next section.

2.2. Evaluation of High-Voltage Performance and Kinetics of Regenerated Materials

Before verifying the high-voltage performance of RLCO material, the electrochemical performance of SLCO, RLCO, and CLCO materials in the normal voltage range of 3.0–4.3 V was first investigated. Due to the structural degradation and Li loss, the SLCO shows a low initial discharge capacity of 21.7 mA h g^{-1} at 1 C (1 C = 150 mA g^{-1}), significant polarization phenomenon and worse rate performance, as shown in **Figure 4**. However, the RLCO exhibits a significantly improved initial discharge capacity as high as 145.6 mA h g^{-1} and improved electrochemical

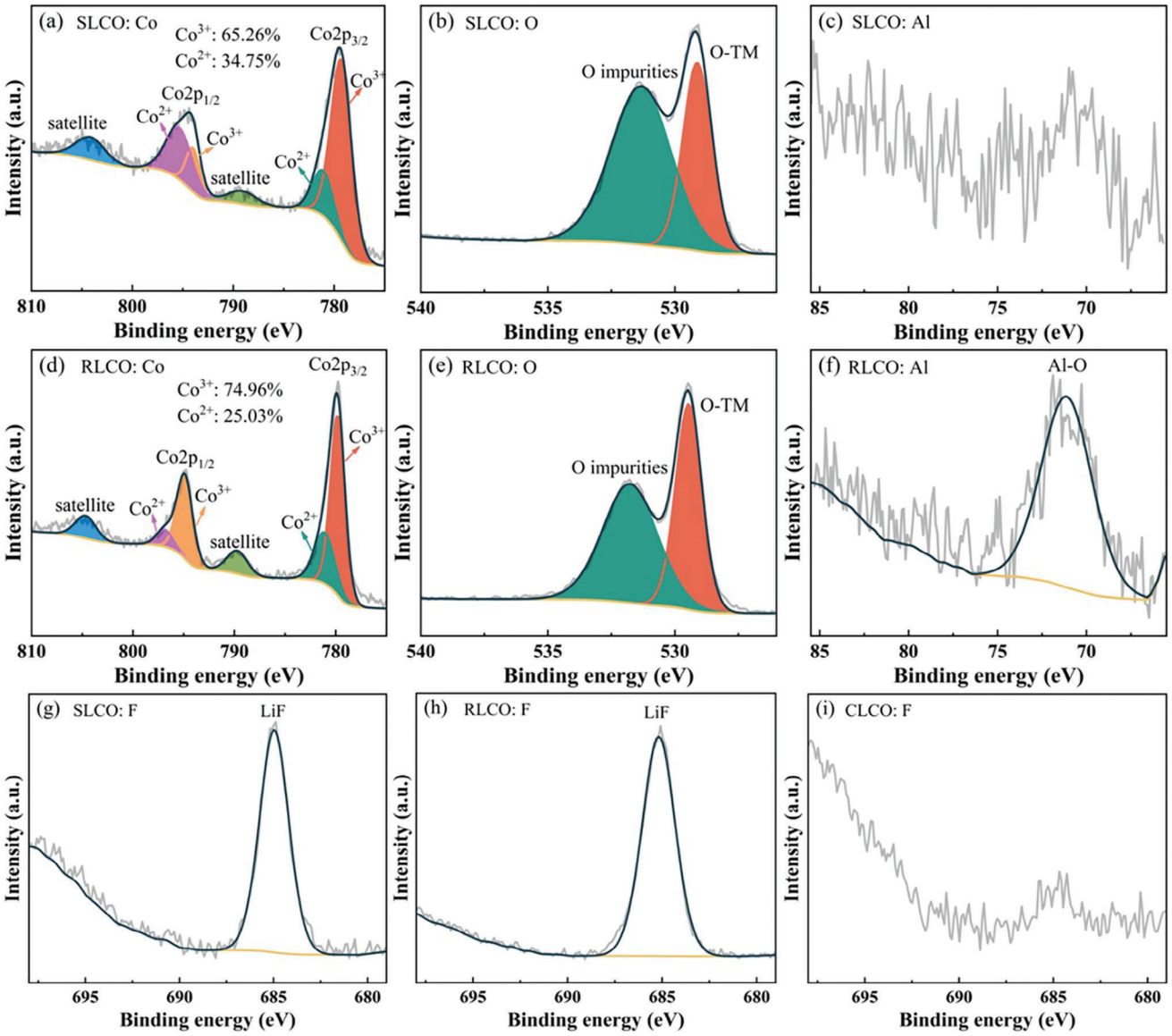

Figure 3. XPS high resolution spectra of Co 2p, O 1s, Al 2p, and F 1s region recorded on SLCO a), b), c) and g), RLCO d), e), f) and h), and CLCO i).

reversibility, which is comparable with CLCO, as shown in Figure 4a,b. In addition, RLCO shows much higher capacity than SLCO and CLCO at various current densities from 0.1 to 5 C, as shown in Figure 4c. Its reversible capacity reaches 121.6 mA h g^{-1} (106.7 mA h g^{-1} for CLCO) even at a high current density of 5 C and recovers to 151.5 mA h g^{-1} (144.8 mA h g^{-1} for CLCO) when the current density returns to 0.1 C. Due to the structural degradation and Li loss, the CV of SLCO material shows a significant polarization phenomenon (Figure S7a, Supporting Information), with almost none of the redox peaks typically observed for LCO. However, RLCO and CLCO materials exhibit typical LCO redox peaks and show good electrochemical reversibility, and the more complex CV curve of RLCO material compared to CLCO material is due to additional phase transition, which may be related to Al doping and LiF coating, as shown in Figure S7b,c (Supporting Information). The electrochemical performance of SLCO material is restored through solid-state synthesis regeneration, and regenerated materials exhibit better rate performance compared to CLCO material, attributed to their more stable crystal structure (resulting from the Al doping and LiF coating). In general, increasing the charging voltage of LIBs above the conventional limit range could improve the discharge capacity, energy density, and working voltage of the battery. However, more than 80% of Li (theoretically) will de-intercalate from the LCO when charged to 4.7 V, often accompanied by O loss and Co dissolution, and the deleterious phase transition of LCO from O3 hexagonal to the H1-3 mixed phase of O1 and O3 structure is more serious, as shown in Figure 4d. If there is no support between the CoO_6 layers, the layered structure of LCO is prone to collapse, further accelerating the unexpected capacity decay.

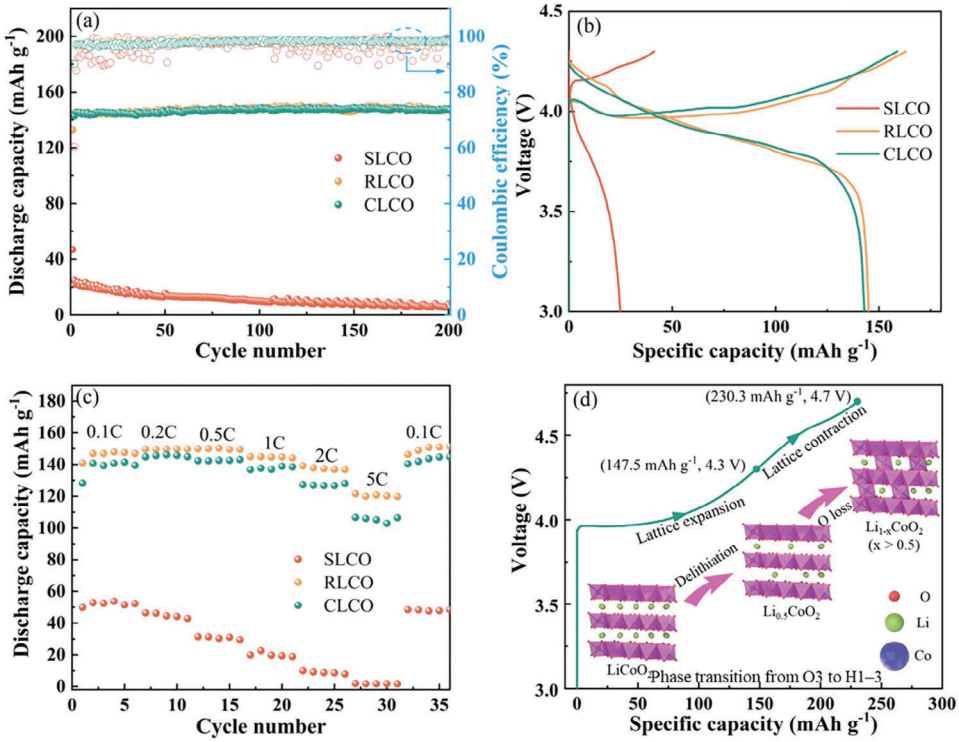

Figure 4. Electrochemical performances of SLCO, RLCO, and CLCO materials recorded at 3.0–4.3 V. a) Cycling performance at 1 C. b) Charge–discharge curves. c) Rate performance. d) Schematic of the phase transition of LCO driven by high voltage.

The high voltage electrochemical performance at 4.5 V of RLCO and CLCO are further compared in **Figure 5**. RLCO material shows an excellent initial discharge capacity of 181 mA h g^{-1} and capacity retention of 80.4% after 400 cycles at a high voltage of 4.5 V. In comparison, CLCO has respective capacity and capacity retention of only 167.6 mA h g^{-1} and 68.5% under the same conditions, as shown in Figure 5a. And RLCO has a comparable rate performance with CLCO, and could still recover to the initial discharge capacity when the current density shifts back to 0.1 C (Figure 5b). Compared to CLCO, RLCO shows a gentle voltage drop during prolonged cycles, indicating low polarization during cycling at high voltage (Figure 5c). In addition, the phase of RLCO and CLCO remains LCO after 200 cycles at high voltages, and no impurity phase is generated, as shown in Figure 5d. The methods for preparing high-voltage electrodes by direct regeneration of spent LCO batteries and their performance are summarized in Figure 5e and Table S3 (Supporting Information). The spent material used in our recovery process is highly degraded with a residual capacity of only 21.7 mA h g^{-1} at 1 C, which is the lowest among all published reports. The restored capacity and capacity retention after 100 cycles of RLCO material are competitive, and the capacity retention slowly decreases to 99.9% after 100 cycles, which is the best result reported for 4.5 V high-voltage LCO involving direct regeneration of spent LCO batteries.[24–26,31,32] Moreover, the electrochemical performance of RLCO material at 4.5 V is even better than that of modified materials of CLCO.[33,34]

Such superior high-voltage performance of RLCO material could also be evidenced by the result of electrochemical impedance spectroscopy (EIS) tests recorded on the electrodes before cycling, as shown in Figure 5f. RLCO shows the smallest charge-transfer impedance (R_{ct} = 169.6 Ω) compared to SLCO (R_{ct} = 617.6 Ω) and CLCO (R_{ct} = 345.3 Ω), demonstrating better electronic conductivity and kinetic performance of RLCO material. In addition, the CV curves at different scanning rates indicate that the major peaks appearing in charge and discharge are caused by the Li^+ extraction and insertion reactions, respectively (Figure 5g,h). Based on the Randles–Sevcik equation:

$$I_p = \left(2.65 \times 10^5\right) n^{3/2} S D_{Li}^{1/2} C_{Li} v^{1/2} \quad (1)$$

where I_p, n, S, D_{Li}, C_{Li}, and v are the peak current, number of electrons, area of the electrode, Li^+ diffusion coefficient, Li^+ concentration in the electrode, and voltage sweep rate, respectively. All I_p are linearly related to the $v^{1/2}$, and the slopes of $I_p/v^{1/2}$ figures are positively related to the D_{Li}, as shown in Figure 5i. The slopes of RLCO material are higher than CLCO material, indicating that the Al doping and LiF coating indeed facilitate the diffusion of Li^+ at high voltage. It is attributed to the fact that the aforementioned expanded interlayer spacing and more stable layered structure of RLCO material have improved the intercalation/extraction efficiency of Li^+ at high voltage. Therefore, the excellent high-voltage electrochemical performance of RLCO material has been confirmed. The LiF coating ensures particle surface stability and resists electrolyte erosion, while Al doping maintains the layered structure of LCO and prevents drastic volume changes, which is crucial for maintaining the effective diffusion path of Li^+ under high voltage. The combination of LiF

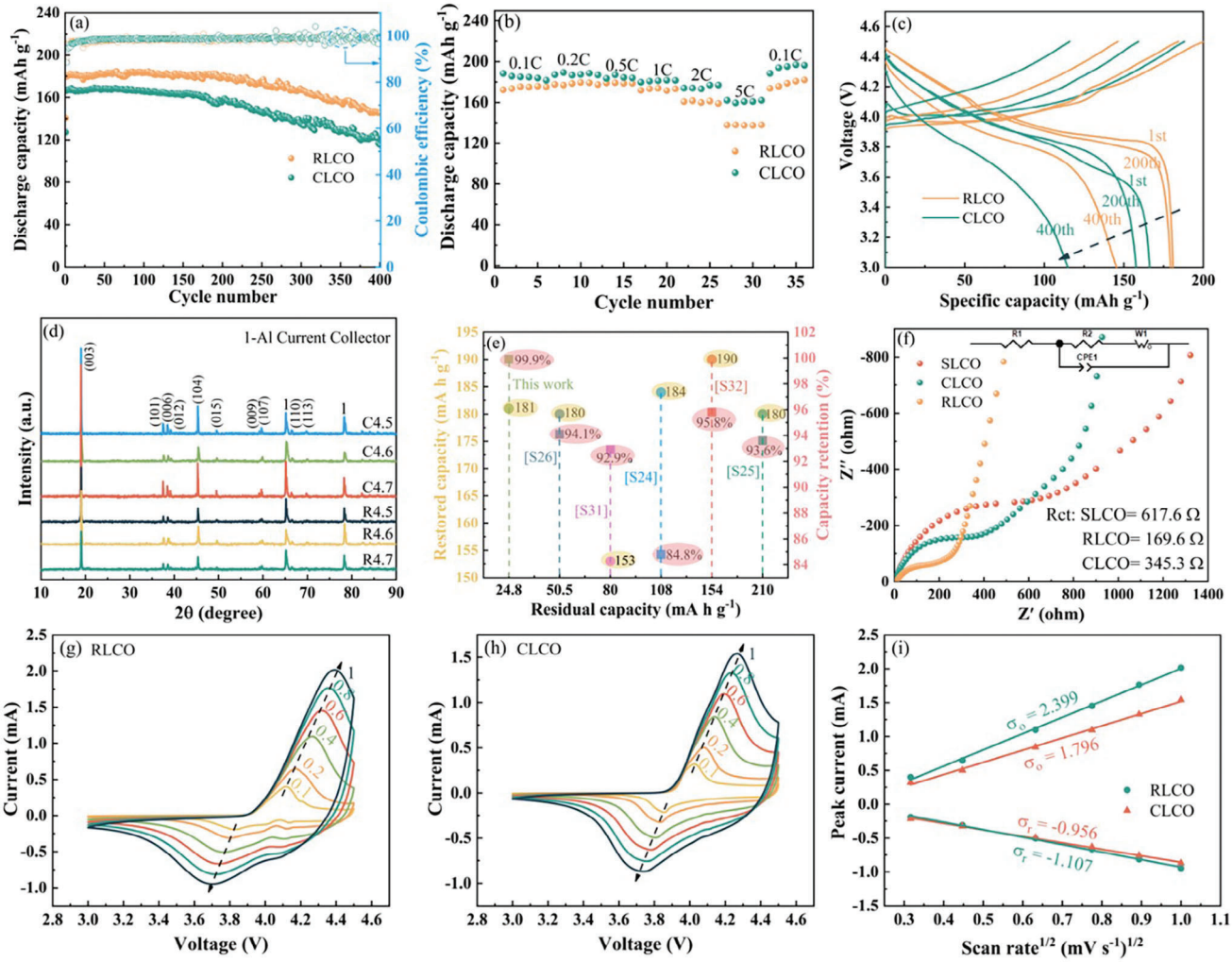

Figure 5. Electrochemical performances of RLCO and CLCO materials at 4.5 V cut-off voltage. a) Cycling performance (1 C). b) Rate performance. c) Charge–discharge curves. d) XRD patterns of RLCO and CLCO after 200 cycles at 4.5, 4.6 and 4.7 V. e) Comparison of electrochemical performances in this work and other published studies. f) Electrochemical impedance spectra (EIS) before cycling. g,h) CV curves at different scan rates of RLCO and CLCO. i) Linear relationship between the major peak currents and scan rates.

coating and Al doping achieves the effect of "the whole is greater than the sum of its parts".

2.3. Theoretical Calculations and Mechanism Analysis

To explore the regeneration mechanism more comprehensively, AlCLCO materials with different mass ratios were prepared under the same conditions to compare the Al doping process between SLCO and CLCO materials. The AlCLCO materials still retain the LCO phase without introducing new impurities, as shown in **Figure** 6a. However, the electrochemical performance of AlCLCO materials at 4.5 V is much lower than that of RLCO material, exhibiting a lower discharge capacity and capacity retention (Figure 6b). Based on this, the diffusion processes of Al in the bulk spent and commercial LCO were further compared by theoretical calculation, as shown in Figure 6c–e. Due to the existence of a large number of Li vacancies in spent materials, Al can spontaneously diffuse into such vacancies, considering that the energy barrier for the Al diffusion into Li vacancies is −1.03 eV. However, due to the structural integrity of CLCO materials, the diffusion of Al into the Li layer needs to overcome a diffusion energy barrier of 1.75 eV, which means that Al doping in commercial materials requires higher energy. Theoretical calculations indicate that the Li vacancies in SLCO materials ($Li_{1-x}CoO_2$) indeed reduce the diffusion hindrance of Al, making it easier to occupy Li sites. The doping of Al in SLCO materials is more uniform, resulting in a more stable RLCO structure and better electrochemical performance than AlCLCO at high voltage.

In conclusion, the closed-loop upgrade and regeneration from spent $Li_{1-x}CoO_2$ materials to high-performing cathode materials have been achieved, as shown in Figure 6f. First, during the pretreatment process, while a trace amount of Al is introduced into the spent materials, a layer of LiF coating is covered on the surface of the spent material particles due to inherent residues and the thermal decomposition of the binder PVDF. Then, due to the

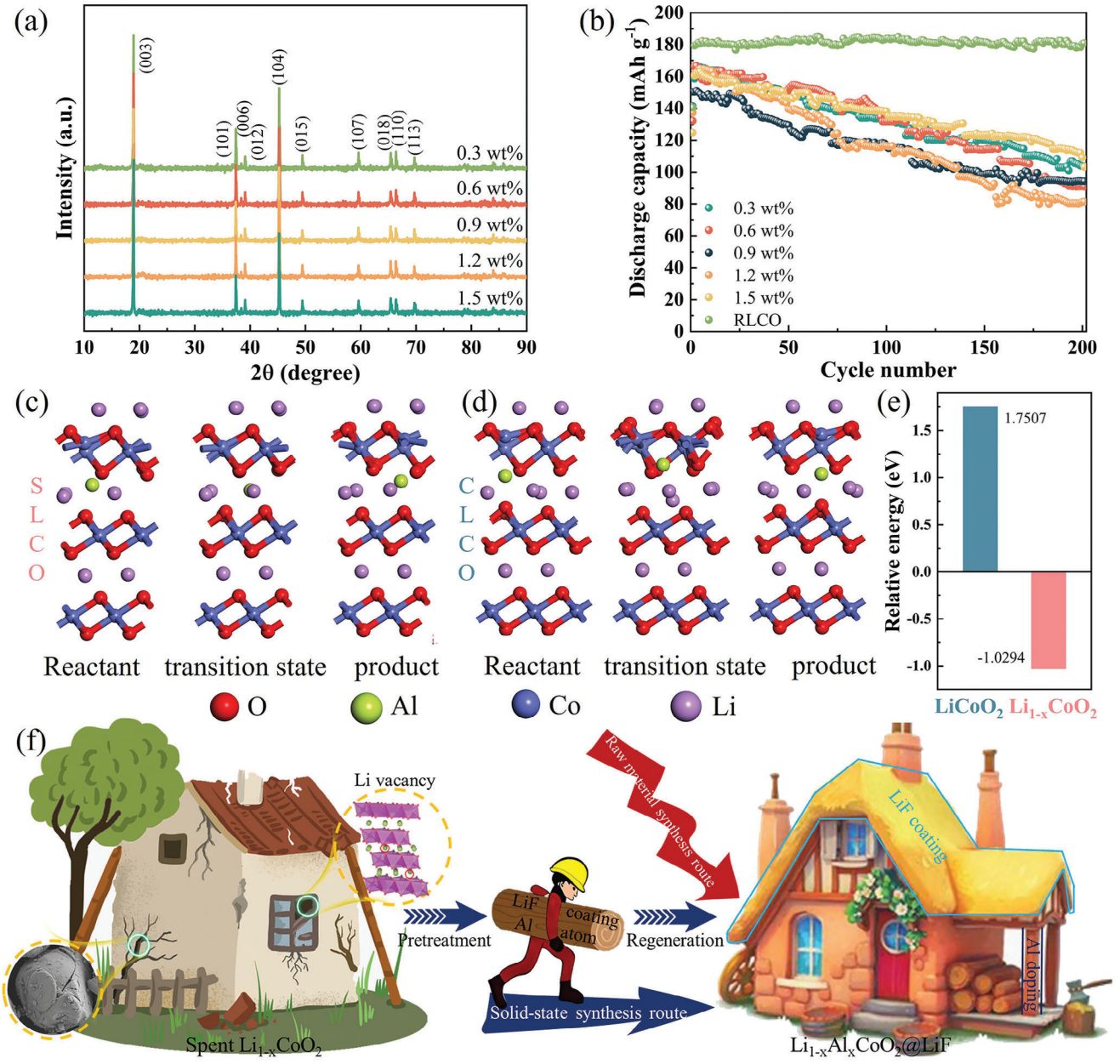

Figure 6. Regeneration mechanism of high-voltage RLCO material. a) XRD patterns of ALCLCO with different Al doping levels. b) Electrochemical performances of ALCLCO with different Al doping levels at 4.5 V cut-off voltage. c,d) Diffusion of Al in bulk SLCO and CLCO e) Diffusion energy barriers of Al in bulk SLCO and CLCO. f) Regeneration mechanism.

thermal stability of LiF and the presence of a large number of Li vacancies in the spent material structure, it is feasible to achieve Al doping while repairing the structure of spent materials during the solid-state regeneration process. On the outside, the LiF coating resists the corrosion caused by the electrolyte, ensuring the stability of the particle surface. Internally, trace amounts of Al diffuse into the regenerated LCO lattice and occupy the Li sites, where they act as pillars between the CoO_6 layers, improving the structural stability of regenerated materials. In addition, compared with the Co—O bond, the Al—O bond formed by lattice-doped Al has higher dissociation energy, which can inhibit the dissolution and diffusion of metal ions in Li layer or electrolyte. Under the dual protection of the external LiF coating and the internal Al doping, the regenerated material can maintain a stable layered structure during long-term cycling at 4.5 V. Moreover, there is no need for the utilization of additional coating/doping agents in the whole closed-loop regeneration process. In contrast to the traditional method of synthesizing high-voltage cathode materials from raw ingredients, the proposed process presents a straightforward, easily accessible, cost-effective, and environmentally friendly approach. This method facilitates the transformation of depleted standard cathode materials into upgraded

4.5 V counterparts, thereby enhancing the energy density of LIBs.

Future research is required. RLCO exhibits higher initial discharge capacities of 207.9 mA h g^{-1} at 4.6 V and 235.8 mA h g^{-1} at 4.7 V than the initial discharge capacities of CLCO material (198 mA h g^{-1} at 4.6 V and 226.4 mA h g^{-1} at 4.7 V), as shown in Figure S8a,b (Supporting Information). However, both RLCO and CLCO materials exhibit poor cycling stability at cut-off voltages of 4.6 and 4.7 V. In this study, the efficacy of Al doping in RLCO during the recycling process for enhancing electrode performance was demonstrated. Further investigation is needed to understand the impact of different Al amounts on the electrode's electrochemical performance and to optimize the doping level. Additionally, future research should focus on modifying both the electrode and/or electrolyte to achieve satisfactory performance at higher voltage values (>4.5 V).

3. Conclusion

A unique route has been proposed to prepare high-performing LCO by directly regenerating spent $Li_{1-x}CoO_2$. The repair of the degraded crystal structure of spent materials and Al doping and LiF coating in situ modification can be achieved in one step by using residual Al impurities from current collectors and high-temperature Li supplementation, directly transforming spent LIBs from hazardous e-waste to high-voltage cathode of LIBs. The dual structure strengthening of Al doping and LiF coating alleviates the surface structure deconstruction of regenerated materials at 4.5 V and enhances the diffusion dynamics of Li^+. Therefore, the regenerated materials exhibit excellent electrochemical performance at a high voltage of 4.5 V. Specifically, the initial discharge capacity of 181 mA h g^{-1} and the capacity retention of 99.9 and 80.4% after 100 and 400 cycles, respectively, could be achieved using the up-graded cathode materials. In addition, through characterizations and theoretical calculations, it is proved that spent materials show superiority in modification compared with commercial materials because of degraded crystal structure and abundant Li vacancies, offering a new path for the development of the next-generation high-performance LIBs accompanied by significant economic and environmental advantages. This recycling strategy could convert end-of-life battery materials into high-performance electrode materials for future application scenarios, which is crucial for promoting the sustainability of battery manufacturing processes.

4. Experimental Section

Regeneration of Spent Cathode Materials: Spent LIBs were collected from spent cell phones in a local recycling center (Shenyang, Liaoning province, P.R. China). Spent LIBs containing graphite anodes and LCO cathodes were discharged (24 h) first in a saturated NaCl solution for safety. After vacuum drying, the spent batteries were separated into organic separators, cathodes, and anodes. The cathode materials powders were separated from Al foils by calcining at 600 °C for 2 h in air, denoted as SLCO. The SLCO powders were repaired using the solid-state synthesis method, and Li_2CO_3 was used as the lithium source. The regenerated materials were defined as RLCO. According to the previous work,[35] the optimal mole ratio n(Li)/n(Co) and the regeneration temperature were selected as 1:1 and 850 °C, respectively. For pyrometallurgical Al doping, Al_2O_3 was used as the doping agent and calcined with CLCO (commercial $LiCoO_2$ material) at different mass ratios in a muffle furnace at 850 °C for 8 h (consistent with the regeneration conditions). The sample obtained was defined as AlCLCO.

Characterizations: The phase composition and crystal structure of different materials were carried out using an X-ray diffractometer (XRD, D8 Bruker, Cu K_α) and the lattice parameters and phase ratio of the target materials were analyzed by the Fullprof software based on the Rietveld refinement. Thermogravimetry and differential scanning calorimetry (TG-DSC, HITACHI STA200, Japan) were used to determine the different stages in the solid-state synthesis process under air atmosphere in the temperature range 30–1000 °C with a ramping rate of 20 °C min^{-1}. The chemical composition of different materials was determined using inductively coupled plasma optical emission spectroscopy (ICP-OES, Optima 8300DV, PerkinElmer, USA). The morphologies and microstructure of the samples were characterized using scanning electron microscopy (SEM, ZEISS GeminiSEM 300, Germany) combined with X-ray dispersive energy spectrometry (EDS) and transmission electron microscope (TEM, JEOL JEM-2100F, Japan). The element valence state on the particle surface was carried out using X-ray photoelectron spectroscopy (XPS, Thermo Scientific K-Alpha, USA).

Electrochemical Characterization: The half-cells (CR2032) were used to test the electrochemical performances of samples. 1 M $LiPF_6$ dissolved in ethylene carbonate: ethyl methyl carbonate: dimethyl carbonate (EC: EMC: DMC, 1:1:1 in volume) was used as the electrolyte, and Celgard 2500 polypropylene membrane was used as the separator. The working electrodes were produced by coating a slurry of active materials, conductive acetylene black, and PVDF with a weight ratio of 8:1:1 on Al foil. The Li sheet was used as an anode. The cycling performance and rate performance were tested using a battery testing system (LAND-CT2001). The test cells were first cycled at 0.1 C for activation before long-term cycling at 1 C. Cyclic voltammogram (CV, 0.2 mV s^{-1}) and electrochemical impedance spectroscopy (EIS, 0.1 MHz-0.01 Hz) were carried out using an electrochemical workstation (CHI660D). In addition, cyclic voltammetry measurements were performed at various scan rates (0.1–1.0 m V s^{-1}) to calculate the Li^+ diffusion coefficient in different materials.

Theoretical Calculations: The theoretical calculations were carried out using the first-principles calculation method based on the density functional theory of plane wave pseudopotential, which was completed in the CASTEP module of Material Studio software. In the calculation, ultrasoft pseudo-potentials were used to describe the interaction between ion core and valence electrons, and the exchange-correlation energy was approximated using the generalized gradient approximation (GGA) in the form of Perdew Burke Ernzerhof (PBE). The plane wave cut-off energy was set at 550 eV, the convergence threshold of ion relaxation total energy was set at 10^{-6} eV, and the interatomic force convergence criterion was 0.03 eV $Å^{-1}$. Also, the k-point grid was set at 5 × 5 × 1. In addition, the Co ($4s^2$), Li ($2s^1$), and Al ($3s^23p^1$) were used as valence electrons, and a vacuum layer (15 Å) was added along the c-axis on the crystal surface to avoid the interlayer coupling caused by periodicity. The spin polarization of the electron was fully considered in the calculation, and the DFT-D method was used for calibration. Furthermore, based on the linear synchronous transit/quadratic synchronous transit (LST/QST), the Ts search was completed through the CASTEP module to determine the diffusion barrier and corresponding migration path of the ion.

Supporting Information

Supporting Information is available from the Wiley Online Library or from the author.

Acknowledgements

This work was supported by the Open Project of theState Key Laboratory of Refractories and Metallurgy, Wuhan University of Science and Technology (G202502), and the National Natural Science Foundation of China (52074084, 52250610222).

Conflict of Interest

The authors declare no conflict of interest.

Data Availability Statement

The data that support the findings of this study are available from the corresponding author upon reasonable request.

Keywords

direct regeneration, high-voltage performance, in situ modification, spent $Li_{1-x}CoO_2$

Received: March 18, 2024
Revised: May 11, 2024
Published online: May 29, 2024

[1] K. Wu, J. Wang, Q. Li, Y. Yang, X. Deng, R. Dang, M. Wu, Z. Wu, X. Xiao, X. Yu, *Nanoscale* **2020**, *12*, 11182.
[2] Y. Bi, J. Tao, Y. Wu, L. Li, Y. Xu, E. Hu, B. Wu, J. Hu, C. Wang, J. Zhang, Y. Qi, J. Xiao, *Science* **2020**, *370*, 1313.
[3] G. Jiang, Y. Zhang, Q. Meng, Y. Zhang, P. Dong, M. Zhang, X. Yang, *ACS Sustainable Chem. Eng.* **2020**, *8*, 18138.
[4] J. Tan, Q. Wang, S. Chen, Z. Li, J. Sun, W. Liu, W. Yang, X. Xiang, X. Sun, X. Duan, *Energy Storage Mater.* **2021**, *41*, 380.
[5] G. Harper, R. Sommerville, E. Kendrick, L. Driscoll, P. Slater, R. Stolkin, A. Walton, P. Christensen, O. Heidrich, S. Lambert, A. Abbott, K. Ryder, L. Gaines, P. Anderson, *Nature* **2019**, *575*, 75.
[6] Y. Tang, B. Zhang, H. Xie, X. Qu, P. Xing, H. Yin, *J. Power Sources* **2020**, *474*, 228596.
[7] M. Chen, X. Ma, B. Chen, R. Arsenault, P. Karlson, N. Simon, Y. Wang, *Joule* **2019**, *3*, 2622.
[8] Y. Bai, N. Muralidharan, Y. Sun, S. Passerini, M. S. Whittingham, I. Belharouak, *Mater. Today* **2020**, *41*, 304.
[9] M. Zheng, J. Wang, S. Qian, Q. Sun, H. Chen, Z. L., Z. Wu, S. Zhang, T. Liu, *ACS Sustainable Chem. Eng.* **2023**, *11*, 4380.
[10] P. Xu, C. Liu, X. Zhang, X. Zheng, W. Lv, F. Rao, P. Yao, J. Wang, Z. Sun, *ACS Sustainable Chem. Eng.* **2021**, *9*, 2271.
[11] C. Yang, J. Zhang, Z. Cao, Q. Jing, Y. Chen, C. Wang, *ACS Sustainable Chem. Eng.* **2020**, *8*, 15732.
[12] Z. Huang, J. Zhu, R. Qiu, J. Ruan, R. Qiu, *J. Cleaner Prod.* **2019**, *229*, 1148.
[13] Y. Zhao, X. Yuan, L. Jiang, J. Wen, H. Wang, R. Guan, J. Zhang, G. Zeng, *Chem. Eng. J.* **2020**, *383*, 123089.
[14] K. Kim, R. Candeago, G. Rim, D. Raymond, A. H. A. Park, X. Su, *iScience* **2021**, *24*, 102374.
[15] J. Wu, M. Zheng, T. Liu, Y. Wang, Y. Liu, J. Nai, L. Zhang, S. Zhang, X. Tao, *Energy Stor. Mater.* **2023**, *54*, 120.
[16] J. Wang, Q. Zhang, J. Sheng, Z. Liang, J. Ma, Y. Chen, G. Zhou, H. Cheng, *Natl Sci Rev* **2022**, *9*, 97.
[17] Y. Yao, M. Zhu, Z. Zhao, B. Tong, Y. Fan, Z. Hua, *ACS Sustainable Chem. Eng.* **2018**, *6*, 10696.
[18] M. Zheng, H. Salim, T. Liu, R. A. Stewart, J. Lu, S. Zhang, *Energy Environ. Sci.* **2021**, *14*, 5801.
[19] K. Fink, S. Santhanagopalan, J. Hartig, L. Cao, *J. Electrochem. Soc.* **2019**, *166*, A3775.
[20] Y. Gao, Y. Li, J. Li, H. Xie, Y. Chen, *J. Alloys Compd.* **2020**, *845*, 156234.
[21] Z. Chi, J. Li, L. Wang, T. Li, Y. Wang, Y. Zhang, S. Tao, M. Zhang, Y. Xiao, Y. Chen, *Green Chem.* **2021**, *23*, 9099.
[22] G. Ji, J. Wang, Z. Liang, K. Jia, J. Ma, Z. Zhuang, G. Zhou, H. Cheng, *Nat. Commun.* **2023**, *14*, 584.
[23] J. B. Goodenough, Y. Kim, *Chem. Mater.* **2010**, *22*, 587.
[24] J. He, Y. Zhang, Y. Zhang, P. Dong, H. Shi, Y. Li, Z. Liang, Y. Xian, J. Duan, D. Wang, *J. Alloys Compd.* **2022**, *908*, 164576.
[25] E. Fan, J. Lin, X. Zhang, R. Chen, F. Wu, L. Li, *Small Methods* **2021**, *5*, 2100672.
[26] J. Wu, J. Lin, E. Fan, R. Chen, F. Wu, L. Li, *ACS Appl. Energy Mater.* **2021**, *4*, 2607.
[27] J. Wang, J. Ma, K. Jia, Z. Liang, G. Ji, Y. Zhao, B. Li, G. Zhou, H. Cheng, *ACS Energy Lett.* **2022**, *7*, 2816.
[28] J. Yang, W. Wang, H. Yang, D. Wang, *Green Chem.* **2020**, *22*, 6489.
[29] C. Xing, H. Da, P. Yang, J. Huang, M. Gan, J. Zhou, Y. Li, H. Zhang, B. Ge, L. Fei, *ACS Nano* **2023**, *17*, 3194.
[30] Z. Chi, J. Li, L. Wang, T. Li, Y. Wang, Y. Zhang, S. Tao, M. Zhang, Y. Xiao, Y. Chen, *Green Chem.* **2021**, *23*, 9099.
[31] Y. Wang, H. Yu, Y. Liu, Y. Wang, Z. Chen, D. Tang, W. Li, J. Li, *Electrochim. Acta* **2022**, *407*, 139863.
[32] J. Wang, K. Jia, J. Ma, Z. Liang, Z. Zhuang, Y. Zhao, B. Li, G. Zhou, H. Cheng, *Nat. Sustain.* **2023**, *6*, 797.
[33] S. Hao, Y. Li, S. Liu, S. Wang, Y. Xiong, X. Ren, G. Cao, J. Zheng, J. Pan, *J. Alloys Compd.* **2022**, *927*, 166843.
[34] Y. Huang, C. Xu, J. Gao, L. Shen, Q. Liu, G. Zhao, Q. Xie, Y. Lin, J. Li, Z. Huang, *Energy Environ. Mater.* **2021**, *6*, e12311.
[35] L. Kong, Z. Li, W. Zhu, C. R. Ratwani, N. Fernando, S. Karunarathne, A. M. Abdelkader, A. R. Kamali, Z. Shi, *J. Colloid Interface Sci.* **2023**, *640*, 179.